# INVESTIGATING THE SPATIAL DEVELOPMENT OF CORROSION OF CORNER-LOCATED STEEL BAR IN CONCRETE BY X-RAY COMPUTED TOMOGRAPHY

Xun Xi[1] and Shangtong Yang[1*]

[1] *Department of Civil and Environmental Engineering, University of Strathclyde, Glasgow, G1 1XJ, United Kingdom.*

## ABSTRACT

In this paper, the chloride-induced corrosion progression of a corner located steel bar in concrete is investigated by X-ray computed tomography (i.e., X-CT). Corrosion of steel bar is accelerated by placing the reinforced specimen in a wetting and drying cyclic corrosive environment, rather than by the impressed current method. 3D X-CT images are obtained and processed to characterize the different material phases, consisting of, steel bar, mortar, corrosion products and voids/cracks. The corrosion products expansion and concrete cracking are analysed and discussed. It has been found that pitting corrosion is prone to appear around the voids close to the steel bar, mainly due to the pre-existing supply of oxygen and moisture. In addition, a distinct transverse crack has been identified which is caused by non-uniform corrosion along the reinforcing steel bar. Within the cross-section, corrosion has also been found non-uniformly distributed, with the maximum rust layer pointing to the corner edge of the sample. Moreover, the corrosion rust distributions are used to parameterize a recently developed non-uniform corrosion model. This experimentally validated non-uniform corrosion model can be applied to corrosion-induced concrete cracking problems with confirmed accuracy. The combination of the use of wetting and drying cyclic corrosive environment and the X-CT scanning can provide a new method to the non-destructive investigation of corrosion process, rust distribution and corrosion-induced concrete cracking in the reinforced concrete structures.

**Keywords:** X-ray CT; phase characterization; non-uniform corrosion; wetting and drying cyclic accelerated corrosion; rust distribution model; concrete structures.

* Corresponding author. Tel: +44 141 548 3273. Email: shangtong.yang@strath.ac.uk.

## 1 INTRODUCTION

Corrosion of the reinforcement in concrete structures is arguably the most significant durability problem, affecting the serviceability and safety of civil engineering structures and infrastructures. It is estimated that the global cost of corrosion is 2.5 trillion US dollars, equivalent to roughly 3.4 percent of the global Gross Domestic Product (GDP) [1]. Corrosion can cause cracking of concrete and de-bonding between the reinforcement and concrete, which may destroy the integrity of concrete cover, reduce the reliability of concrete and lead to premature failure of the structures and infrastructures. Under the climate change, the aging infrastructure will face exacerbated deterioration which warrants new research in understanding the corrosion in civil engineering.

In light of the significance of the problem, over the last few decades, considerable researches have been conducted in understanding the corrosion mechanism [2-4], predicting the structural effect [5-10], preventing the corrosion initiation and propagation [11-14], etc. In particular, a variety of experiments have been carried out in understanding the corrosion phenomena of the reinforcement and the corrosion-induced concrete cracking [15-21]. González et al. [15] investigated the ratio of the maximum pitting penetration to average general penetration for reinforced concrete samples and claimed this ratio could be useful for estimation of the residual life of concrete structures. Moreover, they found the ratio ranged from about 4 to 8 in natural condition and 5 to 13 in electrochemically accelerated corrosion testing condition. Andrade [16] indicated that a negligible loss (e.g., 20 μm) of the cross-section of the reinforcing bar in concrete could lead to a crack width of 0.05-0.1 mm, based on accelerated corrosion tests. Stewart et al. [19, 22] investigated concrete cracking induced by corrosion of multiple reinforcing bars based on electrochemically accelerated corrosion tests. Caré et al. [20] carried out experiments to predict the time to cracking of mortar beams induced by corrosion of

reinforcement. Furthermore, Kashani et al. [21] and Zhang et al. [18] used a 3D optical or laser measurement technique for stochastic corrosion analysis of reinforcing bars. However, in most of these studies, corrosion is accelerated by the impressed current method. In fact, chemical compositions, mass properties and corrosion distribution of the rust are significantly affected by the corrosive environment [3, 23]. The mechanisms of reinforcement corrosion and corrosion-induced concrete cracking in natural environment can be rather different with those corroded by impressed current in electrochemically accelerated corrosion test.

To accurately investigate the corrosion development around the steel bar in concrete, more realistic testing method to accelerate corrosion should be adopted. Wetting and drying cyclic test with the use of chloride solution is the main approach to generate the same corrosion in reinforced concrete as in real environment, especially for coastal reinforced concrete structures which are naturally subjected to wetting and drying cyclic corrosion. Li [24] designed a comprehensive test program to determine the initiation of chloride-induced reinforcement corrosion in concrete structures under salt spray and simultaneous service loads. Fu et al. [25] studied the corrosion characteristics of reinforcement in a 4-year naturally corroded concrete beam. Vidal et al. [26] and Zhang et al. [27] analysed corrosion pattern of reinforcements and surface cracks maps of beams exposed to chloride environment over several years. Yuan and Ji [28] conducted corrosion tests by using artificial environmental chamber and found the corrosion products distribution around the reinforcement is in a semi-elliptical shape. Zhao et al. [29-31] carried out wetting and drying accelerated corrosion tests on reinforced concrete samples and proposed a Gaussian non-uniform corrosion model to quantitatively define the corrosion products distribution. In addition, Ye et al. [32] studied the rust distribution of corner located rebar by accelerating corrosion in artificial environmental chamber. Further, Wong et al. [12] carried out wetting and drying accelerated corrosion tests and found that corrosion

79 products were preferentially deposited in large cracks rather than pore spaces in the cement
80 paste.
81
82 However, to examine the corrosion development within the reinforced concrete samples,
83 almost all existing studies used destructive observation. The destructive observation means the
84 corroded reinforced concrete samples were cut to physically expose the cross section for
85 analysing the corrosion progression between the steel bar and the concrete. It was usually
86 followed by crush of the samples for weighing the mass of the corroded steel to calculate of
87 corrosion degree. This approach has been widely used to help understand the rust properties
88 and distributions [28, 33, 34], the corrosion effect on the steel-concrete interface [35, 36] and
89 the corrosion products expansion behaviour [12, 25, 37] coupled with digital optical
90 microscope, scanning electron microscope (SEM) and energy-dispersive X-ray spectroscopy
91 (EDS). However, the microstructures of the reinforced concrete samples are very likely to be
92 affected or interfered by the cutting, grinding and polishing processes [35]. Moreover, the
93 technician skills, processing procedure and measuring method are also very likely to affect the
94 results.
95
96 Recently, a non-destructive experimental method using X-ray computed tomography (i.e., X-
97 CT), has been applied in medicine and material science research [38, 39]. Meanwhile, the X-
98 CT technique has also been used for studying fracture, pore structures and permeability of
99 concrete [40-43]. The distinct advantage of X-CT test on corrosion of reinforced concrete is
100 the corrosion development, e.g., initiation, propagation and rust distribution, can be imaged
101 without any physical cut or smash. Beck [44] perhaps first applied the X-CT method to
102 investigate the corrosion process of the reinforcing steel in a mortar cylinder with a height of
103 90 mm and a diameter of 40 mm. Michel et al. [45] employed X-CT to study the corrosion

104 products and the formation and propagation of cracks in a reinforced mortar prism sample with
105 a resolution of 75 μm. Šavija et al. [46] investigated the corrosion induced cover cracking in a
106 mortar cylindrical specimen with a diameter of 34.1 mm by X-CT scanning with a resolution
107 of 16 μm. Dong et al. [47] observed the development of steel corrosion, corrosion products
108 formation, as well as the subsequent initiation and propagation of corrosion-induced cracks by
109 X-CT. Itty et al. [48] compared the difference in morphology of corrosion deterioration in the
110 case of carbon steel or stainless steel reinforcement in mortar cylinders.
111
112 A comprehensive literature review suggests that (1) within the limited studies using X-CT for
113 analysing corrosion in concrete structures, all accelerated corrosion tests employed impressed
114 current approach which can generate significantly different corrosion products and distribution;
115 (2) very limited data was presented on corrosion of the corner located reinforcing bar in
116 concrete which had made the modelling work in corrosion of corner located reinforcement hard
117 to be validated; and (3) no non-uniform corrosion model was parameterised based on non-
118 destructive experimental test results, as the destructive approaches might change the structure
119 of the cross section and thus result in inaccurate corrosion distribution.
120
121 This paper investigates the corrosion progression of a corner located steel bar in concrete by
122 X-CT test, under the accelerated wetting and drying cyclic corrosion. X-CT images with rich
123 65,536 grey levels are obtained and then processed by in-house scripts, to reliably characterize
124 the different material phases, consisting of, steel bar, mortar, corrosion products and
125 voids/cracks. The corrosion products expansion behaviors are analysed and discussed; the
126 corrosion degree and the maximum and average radial losses of steel bar along the longitudinal
127 direction are then evaluated. Further, the corrosion progression data obtained from analyzing
128 the X-CT results are used to parameterize a non-uniform corrosion model. This non-uniform

129 corrosion model can then be applied to modelling the corrosion-induced concrete cracking
130 problems with confirmed accuracy.
131
132 **2 X-CT EXPERIMENTATION**

133 **2.1 Specimen**

134 In this paper, a cubic mortar specimen with a steel bar located in the corner is designed as
135 shown in Figure 1. The dimensions of the specimen are 20 mm×20 mm×20 mm and the
136 diameter of the steel bar is 2.94 mm. The thickness of cover from both sides is 4 mm. The
137 specimen mixture proportions are shown in Table 1. Sodium chloride that accounted for 5%
138 by weight of the cement was mixed into the specimens to accelerate the corrosion of steel bar
139 [49]. The specimens were casted into the purpose-made moulds and taken out of the moulds
140 after the initial 24 hours for curing of 28 days. To ensure the oxygen and chloride diffuse from
141 the two sides with the least cover thickness, the other sides were surface treated with protective
142 sealant.
143
144 The specimen was placed into a wetting and drying cyclic environment, which consists of
145 soaking the specimen into 5.8 wt.% sodium chloride solutions for 4 hours and drying for 20
146 hours under about 20% humidity; every 24-hour is a cycle. The temperature for both dry and
147 wet environments is 48 ℃.
148

149 **2.2 X-CT Technique**

150 The corroded specimen was scanned with the Nikon Metrology X-ray micro CT system with
151 225 kV X-ray source (as shown in Figure 2). The X-CT scanning technique is based on the fact
152 that the material can attenuate the X-ray passing through it. The attenuation rate depends on

153 the X-ray energy and the composition of the object. The X-ray system generates a range of
154 energy spectrum (polychromatic beam) and it is not attenuated uniformly when passing through
155 an object. For example, when passing through the centre area of the steel bar, the X-ray would
156 be enhanced compared with that passing through the edges. As such, the edge of the steel bar
157 in the reconstructed image has brighter voxels. The difference of grey value of the voxels at
158 different locations of the steel bar is not caused by the density of the material but the technique
159 itself; such an artefact is known as "beam hardening" or "cupping artefact" [46]. The beam-
160 hardening is impossible to eliminate while it could be reduced by placing a surrounding metal
161 as filter between the X-ray source and the object. The filter can not only reduce the soft X-ray
162 from the source but also reduce the scattering effect. In this study, a 0.25 mm copper filter was
163 used to reduce the effect of beam hardening. Scan parameters were 3141 projections (per scan,
164 angular step 0.1146 degrees), 150 kV, 77 μA, 1000 millisecond exposure. A single scan took
165 about 1 hour with achieved resolution of 16.25 μm.
166

167 **3 X-CT IMAGE PROCESSING AND SEGMENTATION**

168 A 3D structure was numerically reconstructed using the filtered back projection algorithm from
169 Nikon XTekCT software version 4.3.4. The specimens were first scanned to ensure no initial
170 crack existing. Figure 3 shows the reconstructed images of the specimen exposed to the
171 corrosive environment for 112 days. It can be seen that the 3D images of the specimen obtained
172 are not in parallel with the analysing coordinate system. This is very common and these initial
173 images will need to be geometrically reconfigured. In this study, all initial 3D images were
174 geometrically rotated and the air regions were cropped to reduce possible edge effect. Figure 4
175 shows the geometrically processed X-CT images for the corroded sample.
176

177 The X-CT attenuation value is quantified on a grey value scale with 65,536 levels (i.e., 16-bit
178 image), which provide higher quality presentation than 256 levels (8-bit image). In the
179 meantime, the 16-bit image data is much larger than an 8-bit image. Since steel, corrosion
180 products, mortar and voids or cracks have different densities, the attenuation of X-ray will
181 produce different grey values, possibly in a wide range. Figure 5 illustrates the grey values
182 along a probing line which pass through mortar, voids, steel and the corrosion products.
183 Depending on the densities of the materials, the X-CT pictures show different grey value for
184 each of the material phases; the denser material shows the brighter in the X-CT image and has
185 the higher grey value. In Figure 5 (b), the grey values are plotted along the probing line passing
186 all phases, i.e., steel, corrosion products, mortar and voids or cracks. It should be noted that
187 corrosion products are mixed materials consisting of $FeO$ , $Fe_2O_3$ and $Fe_3O_4$ respectively in
188 terms of oxides, , of which the densities vary between 3.3-5.2 g/cm$^3$. In this study, we used trial
189 and error approach coupled with manual check-up to identify the phases at some suspicious
190 points. Once the thresholds are determined, they are then used for segmentation of the raw
191 images.
192
193 By using the segmentation thresholds, the 3D images of the corroded reinforced mortar sample
194 can be separated and recognized in terms of the mortar, steel bar, corrosion products and
195 voids/cracks. Figure 6 shows the 3D images of (a) mortar, (b) steel bar after corrosion, (c)
196 distribution of corrosion products and (d) distribution of voids and cracks around the corner.
197 In Figure 6(a), clearly, there are 2 longitudinal cracks presenting; most interestingly, a
198 transverse crack close to the bottom of the sample also appears. The transverse crack takes
199 place where the most corrosion products are accumulated along the longitudinal direction. This
200 changes our usual understanding that corrosion induced concrete cracking is normally
201 longitudinal cracking, whilst transverse cracks can also be induced by reinforcement corrosion.

Moreover, it has been found that the transverse crack initials from the concrete surface and propagates towards the steel bar. From Figure 6(b) it can be seen the corrosion of the steel bar is non-uniform along both the longitudinal and the circumferential directions. Figure 6(c) shows the accumulation of corrosion products along the reinforcing bar; it should be noted that the thickness of the cylindrical wall significantly varies, though it cannot be clearly observed from this figure and especially the current viewing angle. Figure 6(d) illustrates the pore voids and cracks due to corrosion expansion.

To better analyze the spatial distribution of corrosion, the 3D structure of the corroded sample is cut vertically (i.e., cross section) and longitudinally at a number of locations. Figure 7 shows three typical cross section images around the steel bar at different locations. Some useful observations have been obtained, i.e., (i) pitting corrosion was initiated around voids (Figure 7(a)), (ii) corrosion products penetrated or flowed into the cracks (Figure 7(b)) and (iii) corrosion rust layer was separated (Figure 7(c)). Given abundant supply of oxygen and water which were pre-existed in the voids, corrosion was more prone to occur at the location of the steel bar in contact with large voids. Moreover, the corrosion products had penetrated into the cracks and/or voids during the accumulation process of the rust. Figure 7(c) presents the image for a slice taken from the 3D structure where there was minor corrosion compared with other locations in the same sample at the same time. In this slice, corrosion rust layer separation is observed. Such a separation phenomenon of rust is caused by the stronger expansion in adjacent places.

As shown in Figure (6b), though the concrete cover and the water/oxygen ingress are the same along the reinforcing bar, the corrosion degree varies in the longitudinal direction. This should be commonly expected because, in macro-cell corrosion, some part of the steel bar works as

227 cathode and thus is prohibited of oxidation. To obtain the longitudinal distribution of corrosion,
228 the 3D structure of the sample is vertically cut in a number of angles along line AO, BO, CO
229 and DO as shown in Figure 8. The corner part of the sample has the most severe corrosion and
230 thus these longitudinal cuts in the corner present typical corrosion distribution images along
231 the reinforcement. In Figure 8, the corrosion products are not uniformly distributed along the
232 steel bar. Moreover, a transverse crack is propagated from the surface to the inside. This
233 corrosion-induced transverse crack has probably not been identified before, to the knowledge
234 of the authors. Transverse cracks are usually considered as applied load-induced cracks. In fact,
235 because the corrosion process is non-uniform along the reinforcing bar, other than the well-
236 known longitudinal cracks, a transverse crack is also initiated by the pressure of corrosion
237 expansion. The mechanism is, under the unbalanced pressure in the longitudinal direction, the
238 surface of the concrete around the maximum corrosion location is subjected to tension which
239 causes cracking at the surface first. This mechanism is also evidenced by the fact that the crack
240 is initiated on the surface and then propagated to the inside, as illustrated in Figure 8. This
241 finding indicates that corrosion-induced concrete cracking is a typical three-dimensional
242 fracture process.
243

244 **4 ANALYSIS OF THE X-CT RESULTS**

245 **4.1 Quantification of the Corrosion Loss**

246 By measuring the residual area of the steel bar after corrosion, corrosion degree of the steel bar
247 at any given location can be calculated as follows:

248 $$\eta = \frac{W_0 - W_r}{W_0} \times 100\% \qquad (1)$$

249 where $W_0$ is the original mass of the steel for any given cross section and $W_r$ is the residual
250 mass of the steel for the same cross section of the reinforcing bar.

Figure 9 illustrates the corrosion degree along the longitudinal direction of the steel bar, calculated from 933 slices cut from the 3D CT reconstructed structure. 15mm length structure was chosen for analysis. Clearly, the corrosion degree of the steel bar varies along the reinforcement. The maximum corrosion degree is 7.5% while the minimum corrosion degree is only about 1%. It should be noted that, because the diameter of the steel bar is only 2.94 mm and thus $W_0$ is quite small, the corrosion degree to concrete cracking should become very high. This explains why we have quite large corrosion degree values compared with previous macroscopic corrosion research [30].

The residual cross section of the steel bar significantly influences the failure probability of corroded RC members [17, 18]. The maximum and average radial losses of steel bar for any cross sections can reflect the non-uniform or pitting corrosion nature along the longitudinal direction. The maximum radial loss can be obtained as follows:

$$R_{ml} = \max_{\theta \in [0,2\pi]} \{1 - R_{re}(\theta)\} \tag{2}$$

where $R_{ml}$ is maximum radial loss of the steel bar; $R_{re}$ is residual radius of the steel bar; $\theta$ is the polar angle within the cross section of the steel bar which varies from 0° to 360° by the increment of 1°.

In addition, the average radial loss can be calculated as follows:

$$R_{av} = \frac{\sum_{\theta=0}^{2\pi} (1 - R_{re}(\theta))}{2\pi} \tag{3}$$

Some researchers have tried to describe the localised or pitting corrosion by a ratio of the maximum pitting penetration over the general corrosion depth [15]. A ratio $\beta$ can be defined as follows [15]:

$$\beta = \frac{R_{ml}}{R_{av}} \tag{4}$$

Figure 10 illustrates that the maximum and average radial loss along the reinforcement. The maximum radial loss considerably varies along the longitudinal direction. The maximum value of $R_{ml}$ is 0.22 mm while the corresponding average radial loss is only 0.05mm which reflects severe non-uniformity. According to the definition, the average radial loss has a linear relationship with corrosion degree. Generally, the average radial loss and the maximum radial loss keep the same trend of change. Figure 11 shows the ratio of maximum radial loss to average radial loss of the steel bar along the reinforcement. It can be found that, the ratio varies from about 4 to 13, which has a good agreement with previous researches [15, 50, 51]. In particular, it has been found that, for the cross sections with larger corrosion degree, the ratio is relatively smaller. This is probably because pitting corrosion plays a more important role at the beginning which is mainly induced by pre-existing supply of water and oxygen in surrounding porous zone; as the diffusion ingress proceeds, the general corrosion dominates.

### 4.2 Measurement of the Rust Distribution

The corrosion rust progression towards the concrete cover drives the cracking mechanism of the cover. Therefore, the rust distribution around the reinforcement is very important in assessing and predicting the critical corrosion degree to concrete cracking [29, 52]. Most researchers selected several locations around the rust and approximately measure the rust boundaries [28, 31, 33]. We developed an automatic measuring method for the boundaries of

297 the rust with better accuracy. As shown in Figure 12(a), the original cross section image was
298 first cropped with the steel bar placed in the centre. Then the pixel image was converted to a
299 binary image by choosing the threshold values for corrosion products as shown in Figure 12(b).
300 Some noise in the original image would lead to some small particles or holes presenting in the
301 binary image, which should be filtered. This involves removing some small dots and filling
302 some small gaps (Figure 12(b) – (c)). Further, "closing" algorithm was used to connect close
303 objects and smooth the edge with the least destructive effect to the original boundary shape.
304 The "closing" algorithm performs a dilation operation followed by an erosion operation using
305 a predefined neighbourhood or structuring element [53].
306
307 The processed binary images were then used for rust thickness measurement. As shown in
308 Figure 13, a polar coordinate system was built with its origin located in the centre of the steel
309 bar. The rust thickness was calculated by measuring the distance between the first two points
310 at the black and white boundaries along the radial line. This radial line was rotating against the
311 origin for 360° to obtain the thickness for the whole circumference of the steel bar. The
312 measurement approach was achieved by an in-house script written in Python. It should be noted
313 that the corrosion products flowed into the surrounding cracks were not counted. Figure 13(b)
314 illustrates the radial thickness distribution of the rust. This measurement approach can provide
315 an effective and accurate way to analyze the rust distribution.
316
317 **5 NON-UNIFORM CORROSION MODEL**
318 A non-uniform corrosion model has recently been developed by the authors based on von Mises
319 distribution which is a continuous probability distribution on a circle [52]. This model describes
320 the non-uniform distribution of corrosion rust around the steel bar as a modified function of
321 von Mises distribution. The model is simply composed of three parameters including the

corrosion degree indicator λ, the non-uniform coefficient $k$ and the location of the maximum thickness of the corrosion layer μ. In this paper, the non-uniform corrosion model is parameterised by the experimental data obtained from the novel X-CT analysis. The corrosion rust layer thickness $T_{cl}(\theta)$ around the reinforcing steel bar is formulated as follows:

$$T_{cl}(\theta) = \lambda \frac{e^{k\cos(\theta-\mu)}}{2\pi I_0(k)} \tag{5}$$

where λ is a corrosion degree indicator, $\mu$ is the location where the maximum thickness of corrosion layer appears, $k$ is the non-uniform corrosion coefficient. $I_0(k)$ is the modified Bessel function of order 0, which can be expressed as follows:

$$I_0(k) = \sum_{m=0}^{\infty} \frac{(\frac{k^2}{4})^m}{(m!)^2} \tag{6}$$

Detail of the derivation of the non-uniform corrosion model is not repeated in this paper but if of interest the readers are suggested to refer to the previous study [52].

Figure 14 schematically presents the regression analysis of the von Mises corrosion model fitted with the X-CT data for a few chosen locations. In total, we have fitted the corrosion model for all the cross sections along the longitudinal direction of the sample which has 933 slice cuts. Figure 15 shows the coefficient of determination $R^2$ of the fitting for all these 933 slices. For some part of the sample, the corrosion degree of the steel bar is relatively smaller and pitting corrosion is more significant, the fitting accuracy is not good at all; $R^2$ is below 0.8 after the cross section with the slice number 486. This is the limitation of the derived von Mises non-uniform corrosion model which is mainly focused on the general corrosion. The localised pitting corrosion at very early stage cannot be well interpreted by this model. Having said this, for the cross sections with a large corrosion degree, most values of $R^2$ are larger than 0.9 which demonstrates reasonably good fitting accuracy. Moreover, importantly, the corroded part of the

345 steel bar with large corrosion degree controls the cracking of concrete. Therefore, the von
346 Mises model can well describe the general non-uniform corrosion of corner located steel bar.
347 The fitted non-uniform corrosion model will be very helpful in simulating the corrosion-
348 induced concrete cracking, as a validated analytical representation of the boundary condition.
349
350 The first 486 slice cuts with good fitting results were used for parameterising the von Mises
351 corrosion model. The parameter $k$ is defined as the non-uniform corrosion coefficient. The
352 larger the $k$ is, the corrosion is more non-uniform [52]. Figure 16 shows the fitted parameter $k$
353 along the longitudinal direction. The maximum value of $k$ is about 10.6 and the minimum value
354 of $k$ is about 2.0 and $k$ significantly varies along the reinforcing steel bar. By counting all the
355 values of $k$ along the longitudinal direction of the whole sample, Figure 17 illustrates the
356 frequency/distribution of $k$. It can be found that, $k$ in a range of 3-3.5 accounts for 32% of the
357 total cut cross sections. Also, $k$ in a range of 3-4.5 accounts for 64% of the total cut cross
358 sections. The number of cross sections with $k$ larger than 5 is very small. This finding suggests
359 that the non-uniform corrosion coefficient $k$ might fall within a small realistic range, affected
360 by chloride content, geometry of the RC structures, corrosion degree and surface crack of
361 concrete. More experimental study would be necessary to clarify the effects of different
362 underlying parameters on $k$ and ideally to formulate an analytical function for $k$. The
363 experimental results and the parameterised von Mises corrosion model can be applied to civil
364 engineering practice in predicting the corrosion induced concrete cracking problems.
365
366 The parameter $\mu$ describes the location where the maximum thickness of rust appears. Figure
367 18 illustrates the value of $\mu$ at every cross section of the steel bar. The mean value of $\mu$ is 1.017
368 $\pi$ and the standard deviation is 0.021. The parameter $\mu$ is very close to $\pi$, which indicates that
369 the maximum thickness of rust is facing the concrete corner. For the specimen with corner

370 rebar, chloride can diffuse into the mortar/concrete from both sides. Previous studies on two-
371 dimensional chloride diffusion have indicated that, the chloride concentration near the corner
372 is larger than that at other locations [54, 55].
373
374 It has been theoretically derived that the parameter λ has a linear relationship with corrosion
375 degree $\eta$ [52], shown as follows:
376 $$\lambda = \alpha \pi R \eta \tag{7}$$
377 where $\alpha$ is the ratio of rust expansion to corroded steel bar, $R$ is the radius of steel bar.
378
379 Figure 19 shows the parameter λ along the longitudinal direction. It can be found that, the
380 maximum value of λ is about 0.95 and the minimum value of λ is about 0.3. The fitted value
381 of λ varies with the locations. To verify the relationship between the parameter λ and corrosion
382 degree $\eta$, a linear regression was performed based on measured corrosion data. Figure 20
383 illustrates the fitting result between the corrosion degree $\eta$ and λ. The fitting function can be
384 obtained as follows:
385 $$\lambda = 0.112\eta + 0.115 \tag{8}$$
386 The parameter λ has a linear relationship with the corrosion degree. The coefficient of
387 determination $R^2$ is 0.78. The fitting accuracy for λ is not very good and the main reason could
388 be the amount of corrosion products penetrating into the cracks is not considered in the von
389 Mises model.
390
391 **6 CONCLUSIONS**

392 In this paper, the corrosion of corner-located steel bar in mortar was investigated by X-ray CT
393 scanning. A realistic and accurate algorithm was developed to analyse the corrosion rust

394 distribution around the steel bar. A true wetting and drying cyclic environment was utilised for
395 the accelerated corrosion process. 3D images with advanced 65,536 grey levels (16-bit) were
396 obtained and segmented in terms of concrete, steel bar, corrosion products and voids or cracks.
397 It has been found that pitting corrosion is prone to appear around voids close to steel bar
398 because the pre-existing supply of oxygen and moisture. Moreover, corrosion has been found
399 varying considerably along both the longitudinal direction of the sample and the cross sections.
400 Also, the ratio of maximum to average radial loss of the steel bar differs from about 4 to 13
401 along the reinforcing bar. The rust distribution in the cross sections obtained has been used to
402 parameterise the von Mises corrosion model. The non-uniform coefficient which represents the
403 non-uniformity of the rust distribution has been found tending to fall in the range of 3 – 4.5.
404 The experimentally validated non-uniform corrosion model can be applied to corrosion induced
405 concrete cracking problems with confirmed accuracy. The combination of the use of wetting
406 and drying cyclic corrosive environment and the X-CT scanning can provide a new method to
407 the non-destructive investigation of corrosion process, rust distribution and corrosion-induced
408 concrete cracking in the reinforced concrete structures.
409

410 **ACKNOWLEDGEMENTS**

411 Financial support from the Engineering and Physical Sciences Research Council (EPSRC) with
412 grant number (EP/S005560/1) is gratefully acknowledged. Dr Jie Hou and Dr Fulin Fan have
413 provided useful discussion and their help is also thankfully acknowledged.
414

415 **REFERENCES**

416 [1] I. NACE, International Measures of Prevention, Application and Economics of Corrosion
417 Technology (IMPACT), Houston, Texas. USA, 2016.
418 [2] A. Česen, T. Kosec, A. Legat, Characterization of steel corrosion in mortar by various
419 electrochemical and physical techniques, Corros. Sci. 75 (2013) 47-57.

[3] I. Balafas, C.J. Burgoyne, Environmental effects on cover cracking due to corrosion, Cem. Concr. Res. 40(9) (2010) 1429-1440.
[4] U.M. Angst, B. Elsener, The size effect in corrosion greatly influences the predicted life span of concrete infrastructures, Sci Adv 3(8) (2017) e1700751.
[5] Z.P. Bazant, Physical model for steel corrosion in concrete sea structures - theory, Journal of the Structural Division-ASCE 105(6) (1979) 1137-1153.
[6] K. Bhargava, A.K. Ghosh, Y. Mori, S. Ramanujam, Model for cover cracking due to rebar corrosion in RC structures, Eng. Struct. 28(8) (2006) 1093-1109.
[7] S.T. Yang, K.F. Li, C.Q. Li, Numerical determination of concrete crack width for corrosion-affected concrete structures, Comput. Struct. 207 (2018) 75-82.
[8] X. Xi, S. Yang, C.Q. Li, M. Cai, X. Hu, Z.K. Shipton, Meso-scale mixed-mode fracture modelling of reinforced concrete structures subjected to non-uniform corrosion, Eng. Fract. Mech. 199 (2018) 114-130.
[9] C.Q. Li, S.T. Yang, M. Saafi, Numerical simulation of behavior of reinforced concrete structures considering corrosion effects on bonding, J. Struct. Eng. 140(12) (2014) 04014092.
[10] C.Q. Li, S.T. Yang, Prediction of concrete crack width under combined reinforcement corrosion and applied load, J. Eng. Mech. 137(11) (2011) 722-731.
[11] R.E. Melchers, C.Q. Li, Reinforcement corrosion initiation and activation times in concrete structures exposed to severe marine environments, Cem. Concr. Res. 39(11) (2009) 1068-1076.
[12] H.S. Wong, Y.X. Zhao, A.R. Karimi, N.R. Buenfeld, W.L. Jin, On the penetration of corrosion products from reinforcing steel into concrete due to chloride-induced corrosion, Corros. Sci. 52(7) (2010) 2469-2480.
[13] X. Xi, S. Yang, Time to surface cracking and crack width of reinforced concrete structures under corrosion of multiple rebars, Constr. Build. Mater. 155 (2017) 114-125.
[14] S. Yang, X. Xi, K. Li, C.-Q. Li, Numerical Modeling of Nonuniform Corrosion-Induced Concrete Crack Width, J. Struct. Eng. 144(8) (2018) 04018120.
[15] J.A. González, C. Andrade, C. Alonso, S. Feliu, Comparison of rates of general corrosion and maximum pitting penetration on concrete embedded steel reinforcement, Cem. Concr. Res. 25(2) (1995) 257-264.
[16] C. Andrade, F.J. Molina, C. Alonso, Cover cracking as a function of rebar corrosion: Part 1-experiment test, Mater. Struct. 26 (1993) 453-454.
[17] M.G. Stewart, Spatial variability of pitting corrosion and its influence on structural fragility and reliability of RC beams in flexure, Struct. Saf. 26(4) (2004) 453-470.
[18] W.P. Zhang, B.B. Zhou, X.L. Gu, H.C. Dai, Probability Distribution Model for Cross-Sectional Area of Corroded Reinforcing Steel Bars, J. Mater. Civ. Eng. 26(5) (2014) 822-832.
[19] J.A. Mullard, M.G. Stewart, Corrosion-induced cover cracking: new test data and predictive models, ACI Structural Journal 108(1) (2011) 71-79.
[20] S. Caré, Q.T. Nguyen, K. Beddiar, Y. Berthaud, Times to cracking in reinforced mortar beams subjected to accelerated corrosion tests, Mater. Struct. 43(1-2) (2009) 107-124.
[21] M.M. Kashani, A.J. Crewe, N.A. Alexander, Use of a 3D optical measurement technique for stochastic corrosion pattern analysis of reinforcing bars subjected to accelerated corrosion, Corros. Sci. 73 (2013) 208-221.
[22] K. Vu, M.G. Stewart, J. Mullard, Corrosion-induced cracking: Experimental data and predictive models, ACI Structural Journal 102(5) (2005) 719-726.
[23] K. Suda, S. Misra, K. Motohashi, Corrosion products of reinforcing bars embedded in concrete, Corros. Sci. 35(5) (1993) 1543-1549.
[24] C.Q. Li, Initiation of chloride-induced reinforcement corrosion in concrete structural members - Experimentation, Aci Structural Journal 98(4) (2001) 502-510.

469 [25] C. Fu, N. Jin, H. Ye, X. Jin, W. Dai, Corrosion characteristics of a 4-year naturally
470 corroded reinforced concrete beam with load-induced transverse cracks, Corros. Sci. 117
471 (2017) 11-23.
472 [26] T. Vidal, A. Castel, R. François, Analyzing crack width to predict corrosion in reinforced
473 concrete, Cem. Concr. Res. 34(1) (2004) 165-174.
474 [27] R. Zhang, A. Castel, R. François, Concrete cover cracking with reinforcement corrosion
475 of RC beam during chloride-induced corrosion process, Cem. Concr. Res. 40(3) (2010) 415-
476 425.
477 [28] Y. Yuan, Y. Ji, Modeling corroded section configuration of steel bar in concrete structure,
478 Constr. Build. Mater. 23(6) (2009) 2461-2466.
479 [29] Y. Zhao, A.R. Karimi, H.S. Wong, B. Hu, N.R. Buenfeld, W. Jin, Comparison of uniform
480 and non-uniform corrosion induced damage in reinforced concrete based on a Gaussian
481 description of the corrosion layer, Corros. Sci. 53(9) (2011) 2803-2814.
482 [30] Y. Zhao, J. Yu, B. Hu, W. Jin, Crack shape and rust distribution in corrosion-induced
483 cracking concrete, Corros. Sci. 55 (2012) 385-393.
484 [31] Y. Zhao, X. Zhang, H. Ding, W. Jin, Non-uniform distribution of a corrosion layer at a
485 steel/concrete interface described by a Gaussian model, Corros. Sci. 112 (2016) 1-12.
486 [32] H. Ye, N. Jin, C. Fu, X. Jin, Rust distribution and corrosion-induced cracking patterns of
487 corner-located rebar in concrete cover, Constr. Build. Mater. 156 (2017) 684-691.
488 [33] Y. Zhao, B. Hu, J. Yu, W. Jin, Non-uniform distribution of rust layer around steel bar in
489 concrete, Corros. Sci. 53(12) (2011) 4300-4308.
490 [34] Y. Zhao, J. Dong, H. Ding, W. Jin, Shape of corrosion-induced cracks in recycled
491 aggregate concrete, Corros. Sci. 98 (2015) 310-317.
492 [35] F. Chen, C.Q. Li, H. Baji, B. Ma, Quantification of steel-concrete interface in reinforced
493 concrete using Backscattered Electron imaging technique, Constr. Build. Mater. 179 (2018)
494 420-429.
495 [36] Y. Zhao, X. Zhang, W. Jin, Influence of environment on the development of corrosion
496 product-filled paste and a corrosion layer at the steel/concrete interface, Corros. Sci. 124 (2017)
497 1-9.
498 [37] J. Ming, J. Shi, W. Sun, Effect of mill scale on the long-term corrosion resistance of a low-
499 alloy reinforcing steel in concrete subjected to chloride solution, Constr. Build. Mater. 163
500 (2018) 508-517.
501 [38] Y. Zhao, Y. Sun, S. Liu, Z. Chen, L. Yuan, Pore structure characterization of coal by
502 synchrotron radiation nano-CT, Fuel 215 (2018) 102-110.
503 [39] J.M. Minto, Q. Tan, R.J. Lunn, G. El Mountassir, H. Guo, X. Cheng, 'Microbial mortar'-
504 restoration of degraded marble structures with microbially induced carbonate precipitation,
505 Constr. Build. Mater. 180 (2018) 44-54.
506 [40] W. Trawiński, J. Bobiński, J. Tejchman, Two-dimensional simulations of concrete
507 fracture at aggregate level with cohesive elements based on X-ray μCT images, Eng. Fract.
508 Mech. 168 (2016) 204-226.
509 [41] K.N. Manahiloh, B. Muhunthan, M. Kayhanian, S.Y. Gebremariam, X-Ray Computed
510 Tomography and Nondestructive Evaluation of Clogging in Porous Concrete Field Samples, J.
511 Mater. Civ. Eng. 24(8) (2012) 1103-1109.
512 [42] X. Sun, Q. Dai, K. Ng, Computational investigation of pore permeability and connectivity
513 from transmission X-ray microscope images of a cement paste specimen, Constr. Build. Mater.
514 68 (2014) 240-251.
515 [43] T. Liu, S. Qin, D. Zou, W. Song, J. Teng, Mesoscopic modeling method of concrete based
516 on statistical analysis of CT images, Constr. Build. Mater. 192 (2018) 429-441.
517 [44] M. Beck, J. Goebbels, A. Burkert, Application of X-ray tomography for the verification
518 of corrosion processes in chloride contaminated mortar, Mater. Corros. 58(3) (2007) 207-210.

519 [45] A. Michel, B.J. Pease, M.R. Geiker, H. Stang, J.F. Olesen, Monitoring reinforcement
520 corrosion and corrosion-induced cracking using non-destructive x-ray attenuation
521 measurements, Cem. Concr. Res. 41(11) (2011) 1085-1094.
522 [46] B. Šavija, M. Luković, S.A.S. Hosseini, J. Pacheco, E. Schlangen, Corrosion induced
523 cover cracking studied by X-ray computed tomography, nanoindentation, and energy
524 dispersive X-ray spectrometry (EDS), Mater. Struct. 48(7) (2014) 2043-2062.
525 [47] B. Dong, G. Fang, Y. Liu, P. Dong, J. Zhang, F. Xing, S. Hong, Monitoring reinforcement
526 corrosion and corrosion-induced cracking by X-ray microcomputed tomography method, Cem.
527 Concr. Res. 100 (2017) 311-321.
528 [48] P.A. Itty, M. Serdar, C. Meral, D. Parkinson, A.A. MacDowell, D. Bjegović, P.J.M.
529 Monteiro, In situ 3D monitoring of corrosion on carbon steel and ferritic stainless steel
530 embedded in cement paste, Corros. Sci. 83 (2014) 409-418.
531 [49] J. Jiang, Y. Yuan, Prediction model for the time-varying corrosion rate of rebar based on
532 micro-environment in concrete, Constr. Build. Mater. 35 (2012) 625-632.
533 [50] B.S. Jang, B.H. Oh, Effects of non-uniform corrosion on the cracking and service life of
534 reinforced concrete structures, Cem. Concr. Res. 40(9) (2010) 1441-1450.
535 [51] B. Šavija, M. Luković, J. Pacheco, E. Schlangen, Cracking of the concrete cover due to
536 reinforcement corrosion: A two-dimensional lattice model study, Constr. Build. Mater. 44
537 (2013) 626-638.
538 [52] X. Xi, S. Yang, C.Q. Li, A non-uniform corrosion model and meso-scale fracture
539 modelling of concrete, Cem. Concr. Res. 108 (2018) 87-102.
540 [53] S. Chen, R.M. Haralick, Recursive erosion, dilation, opening, and closing transforms,
541 IEEE Trans Image Process 4(3) (1995) 335-45.
542 [54] L. Jin, R. Zhang, X. Du, Y. Li, Investigation on the cracking behavior of concrete cover
543 induced by corner located rebar corrosion, Eng. Failure Anal. 52 (2015) 129-143.
544 [55] L.F. Yang, Z. Chen, Q. Gao, J.W. Ju, Compensation length of two-dimensional chloride
545 diffusion in concrete using a boundary element model, Acta Mechanica 224(1) (2012) 123-
546 137.
547

548 **LIST OF TABLES**



550

551 Table 1 Specimen mixture design

| Cement ($kg/m^3$) | Water ($kg/m^3$) | Sand ($kg/m^3$) | Water/cement |
|---|---|---|---|
| 825 | 330 | 825 | 0.4 |

552

## LIST OF FIGURES

19. Fitting parameter λ for the general corrosion part of the steel bar along the longitudinal direction

20. Relationship between the corrosion degree η and the fitting parameter λ

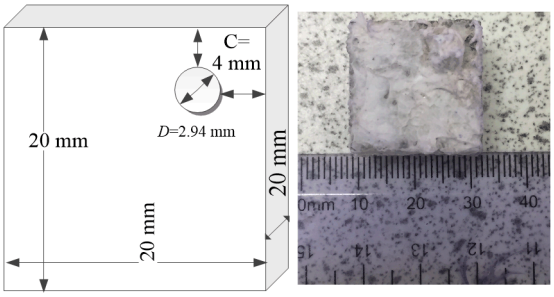


581

582 Figure 1 Schematic of the reinforced mortar specimen

583

584

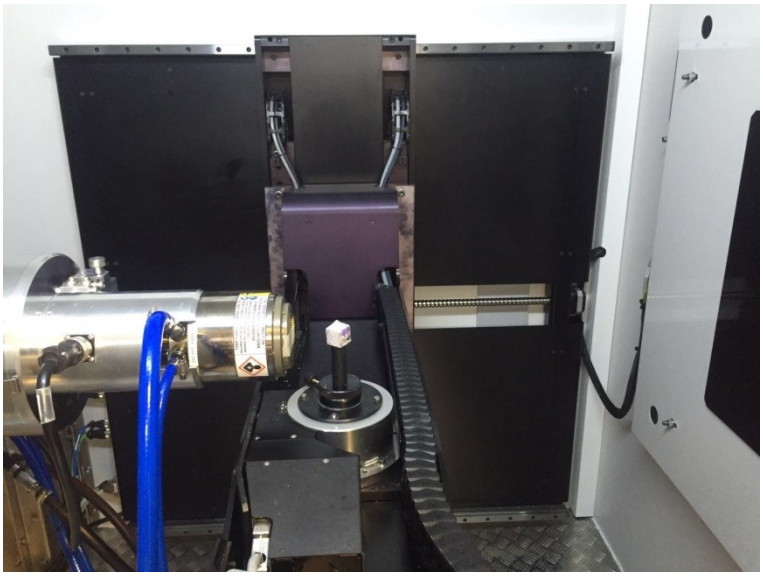

585 Figure 2 Nikon metrology X-ray CT system used in this test

586

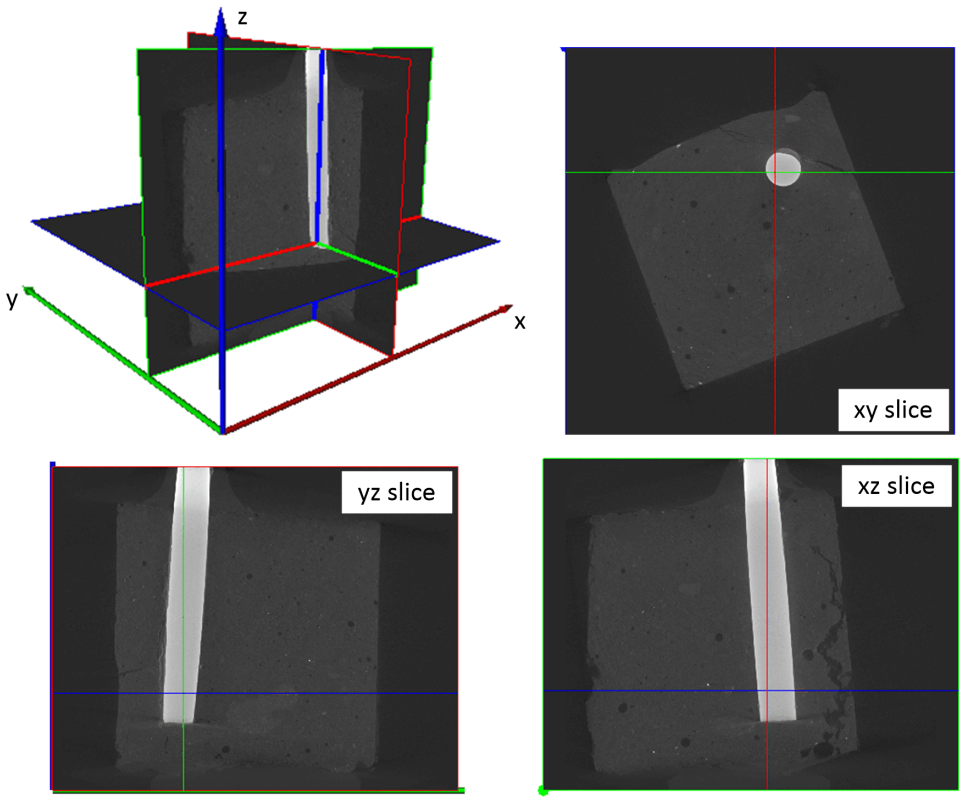


587

588 Figure 3 Typical initial scanning images

589

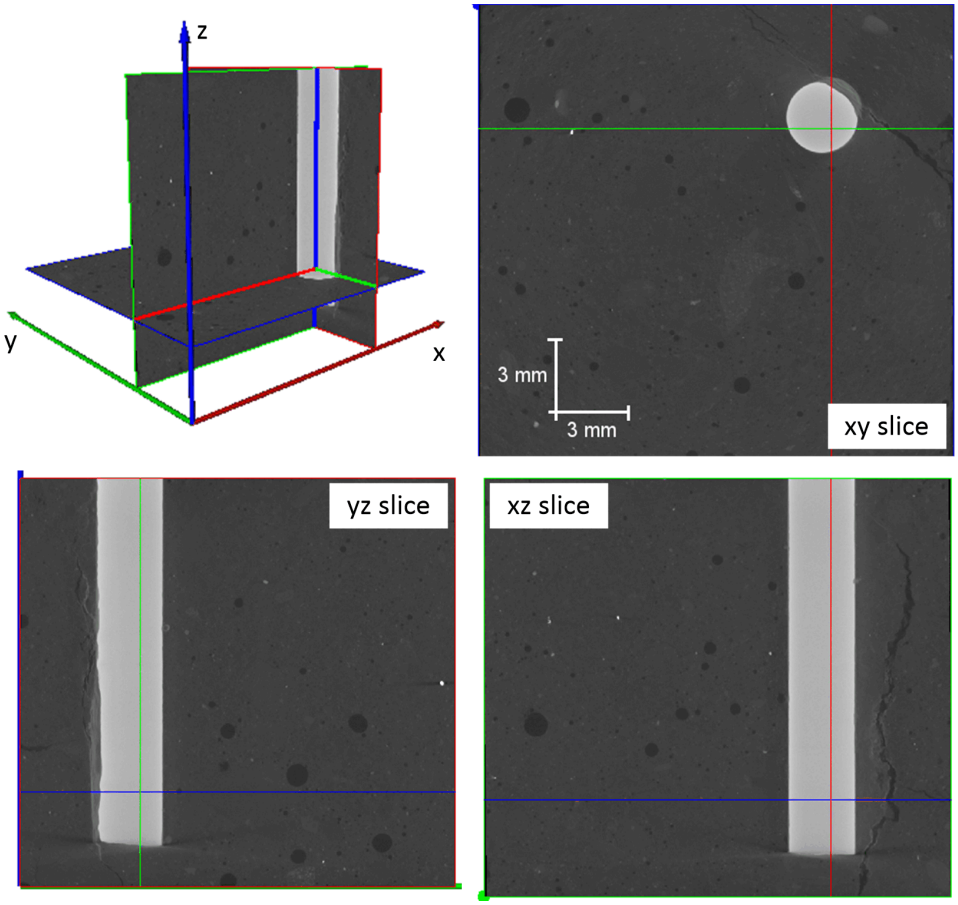


590

591 Figure 4 Geometrically processed images

592

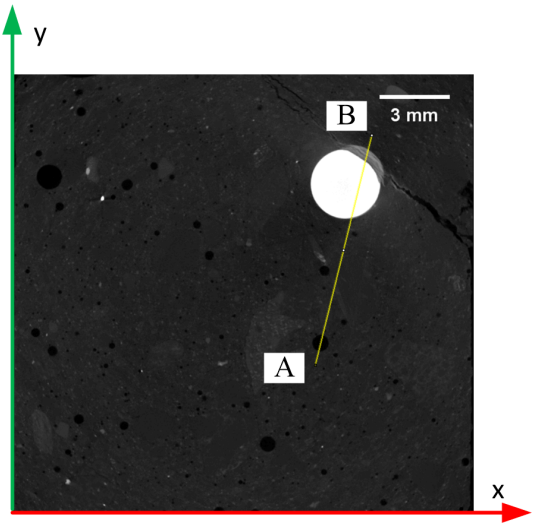


(a) A typical probing line

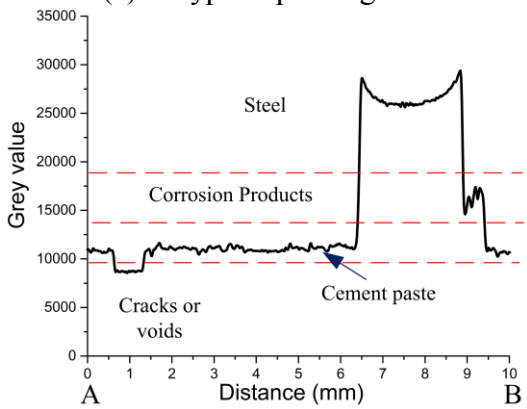


(b) Grey values along the probing line

Figure 5 Phase recognition in the X-CT image

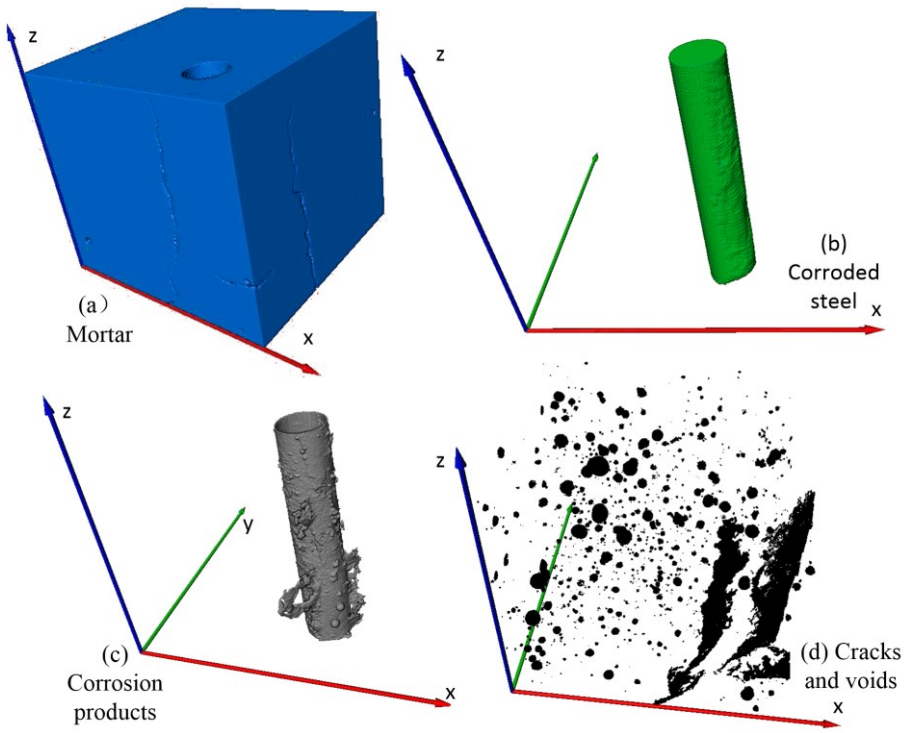


600

601 Figure 6 Three-dimensional views of (a) mortar, (b) corroded steel, (c) corrosion products

602 and (d) cracks and voids

603

604

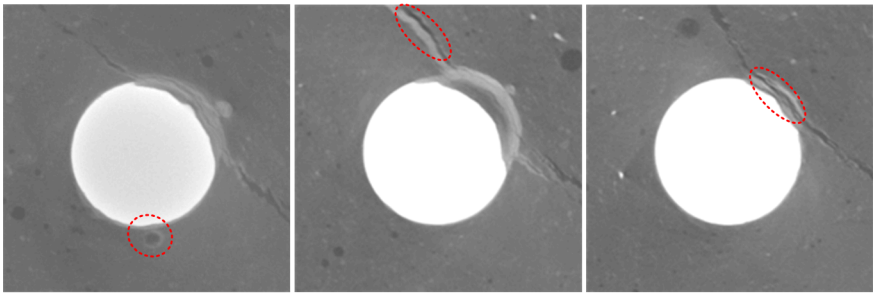

605 （a) Slice 7 （b) Slice 245 （c) Slice 500

606 Figure 7 Typical cross section images around the steel bar

607

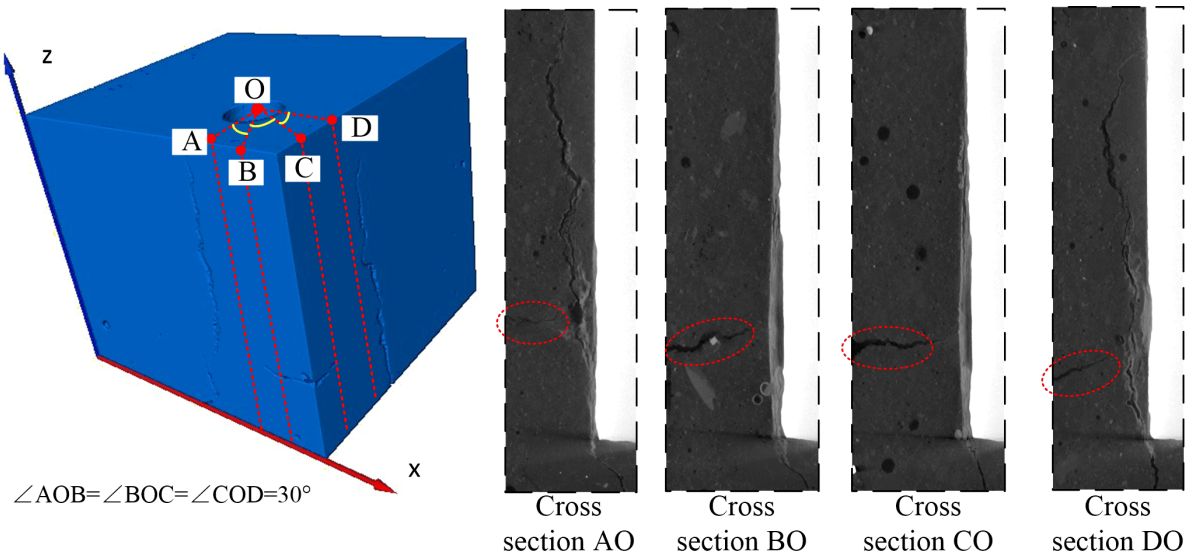


608

609 Figure 8 Longitudinal cuts in the 3D reconstructed structure around the steel bar

610

611

612

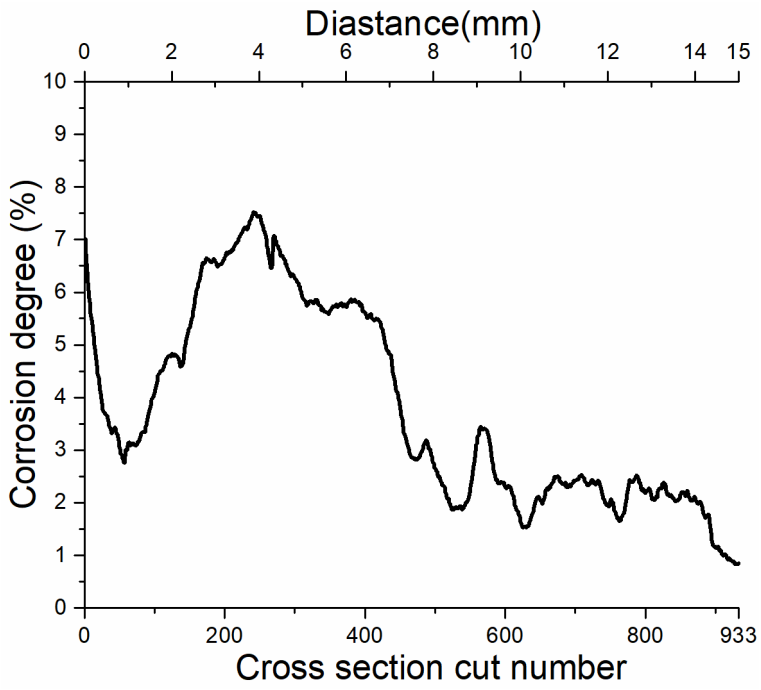


613

614 Figure 9 Corrosion degree of the steel bar along the longitudinal direction

615

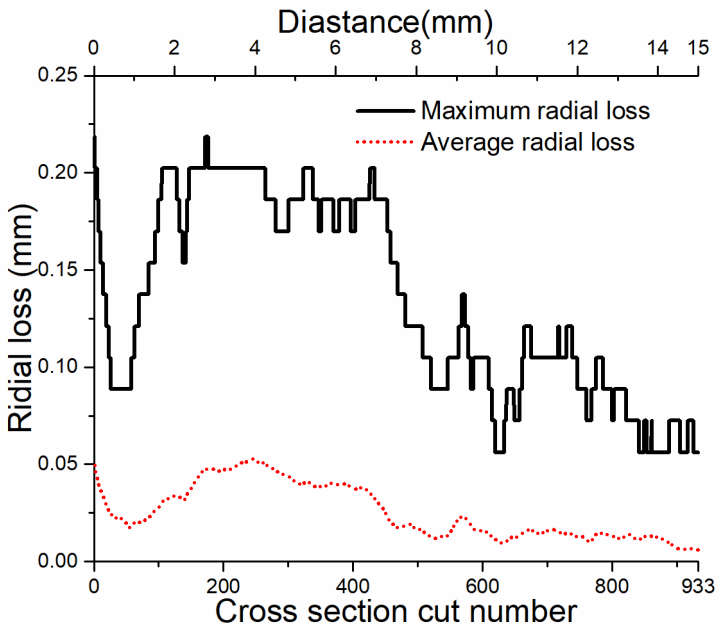


616

617 Figure 10 Maximum and average radial losses of the steel bar along the longitude direction

618

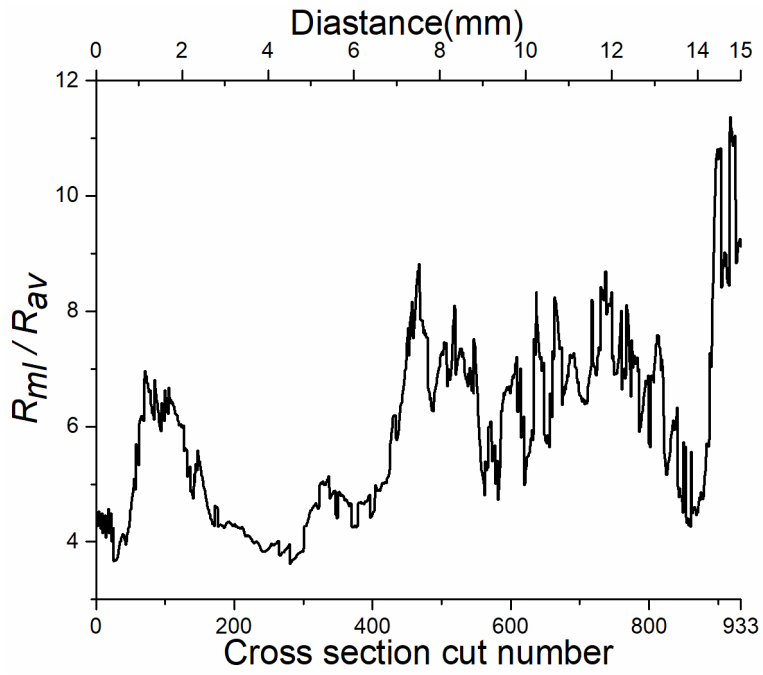


619

620 Figure 11 Ratios of maximum radial loss to average radial loss of the steel bar along the

621 longitudinal direction

622

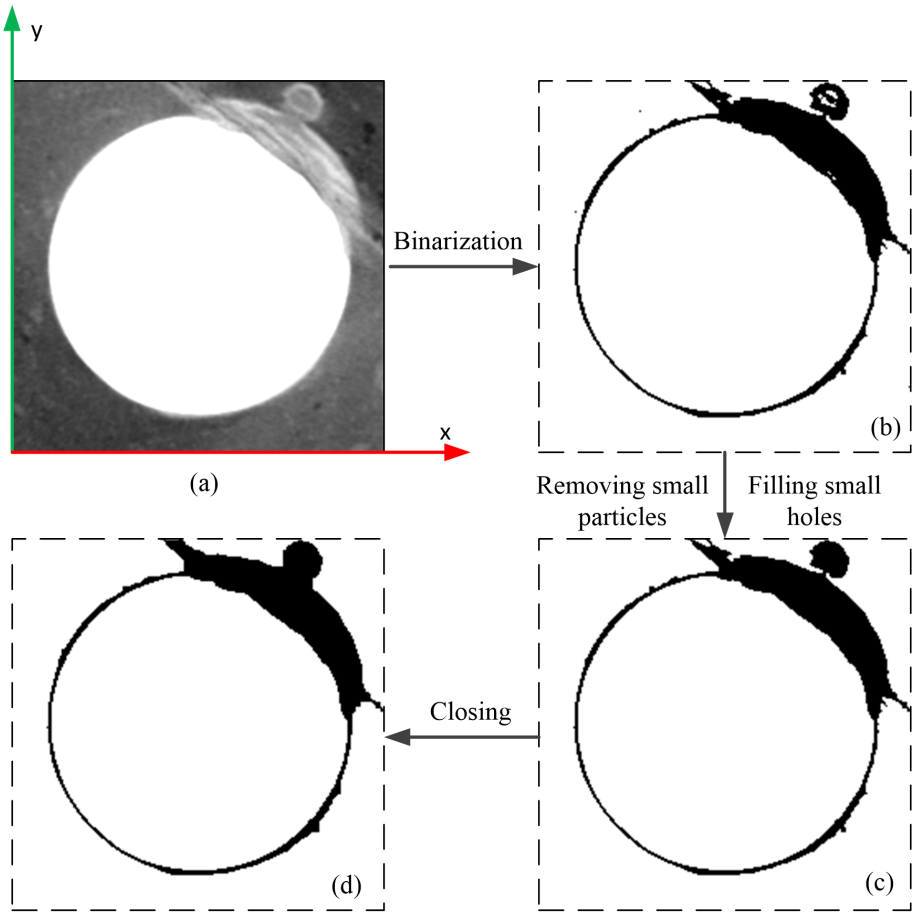


Figure 12 Image processing procedures for rust distribution analysis

627

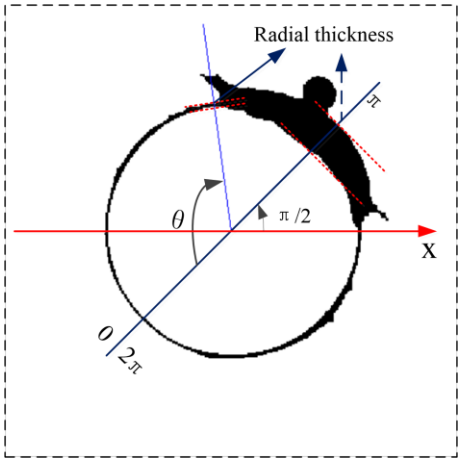


628 (a)

629

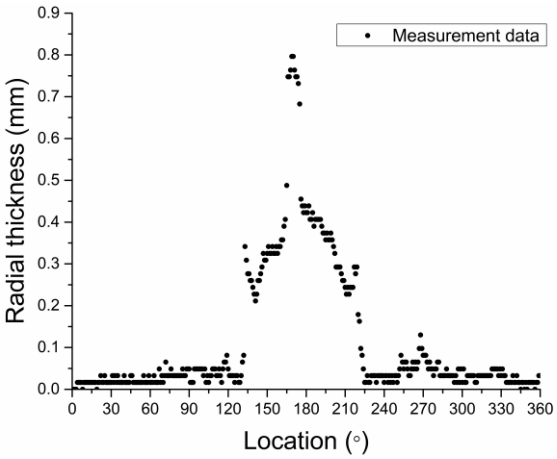


630 (b)

631 Figure 13 Radial thickness measurement of the rust along the circumference of the steel bar

632

633

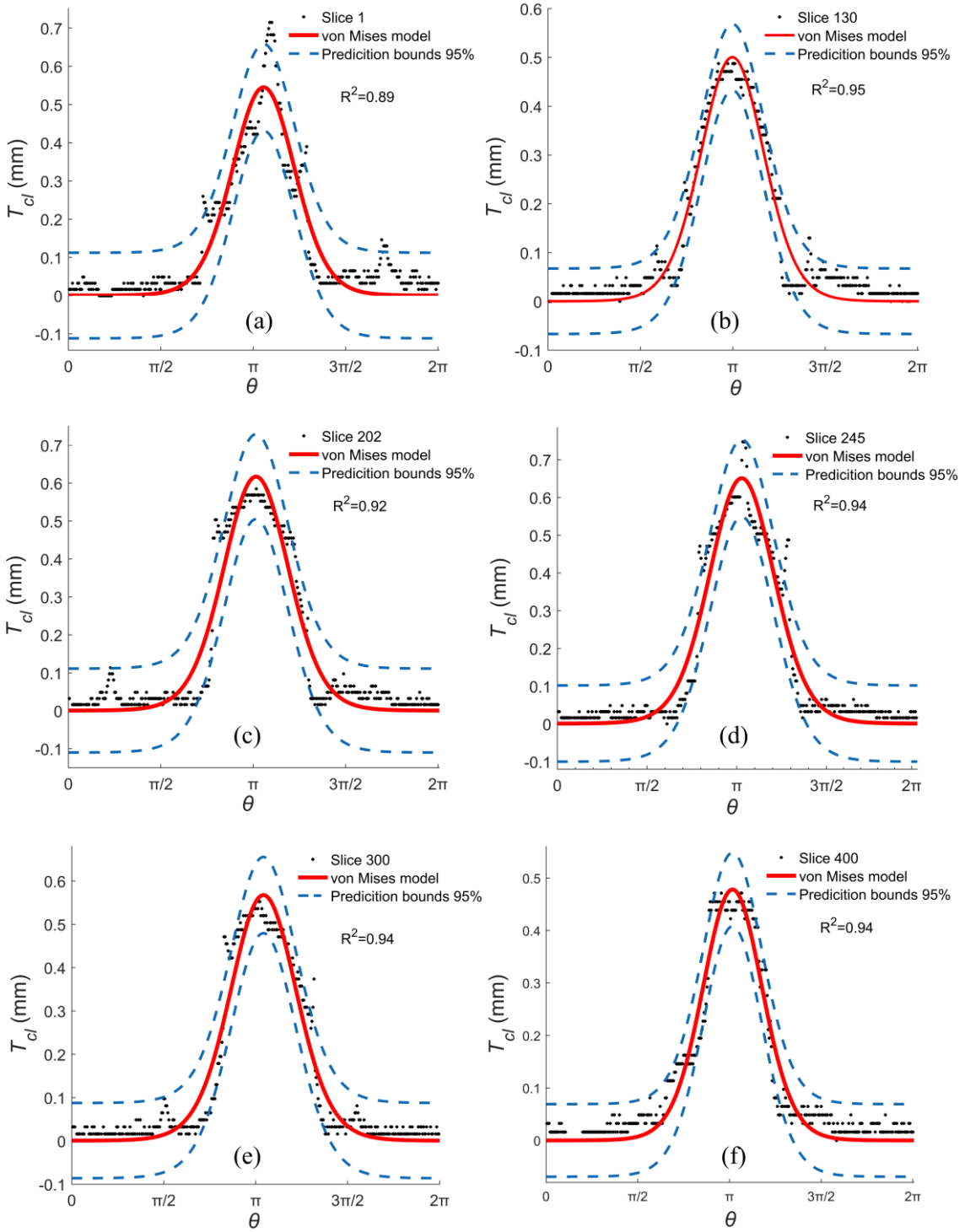


Figure 14 Regression analysis of von Mises corrosion model with the X-CT data

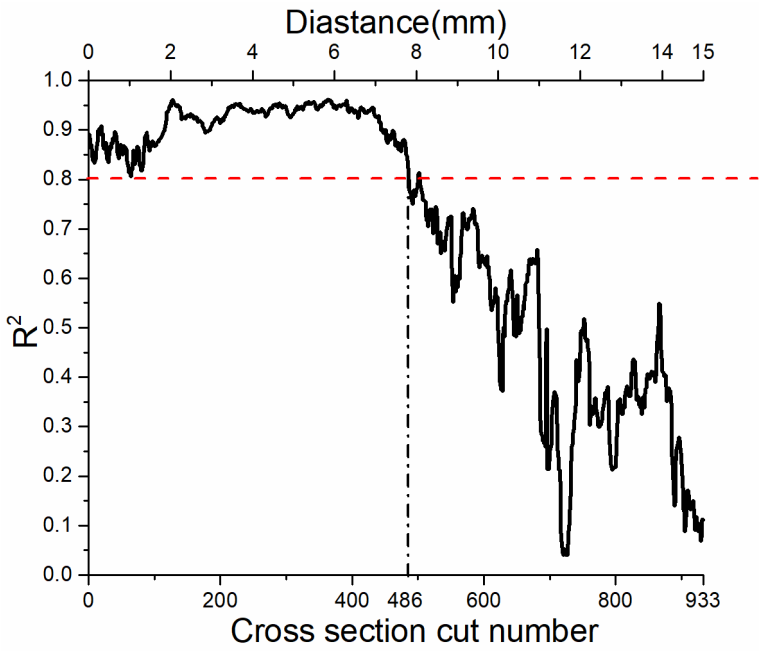


636

637 Figure 15 Coefficient of determination $R^2$ of fitting results from 933 cuts along the

638 longitudinal direction

639

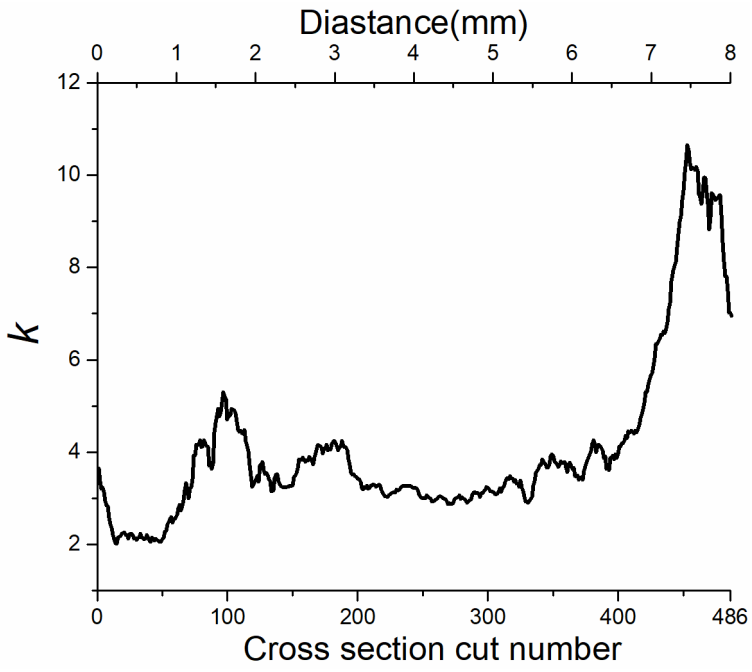


640

641 Figure 16 Non-uniform corrosion coefficient *k* for the general corrosion part of the steel bar

642 along the longitudinal direction

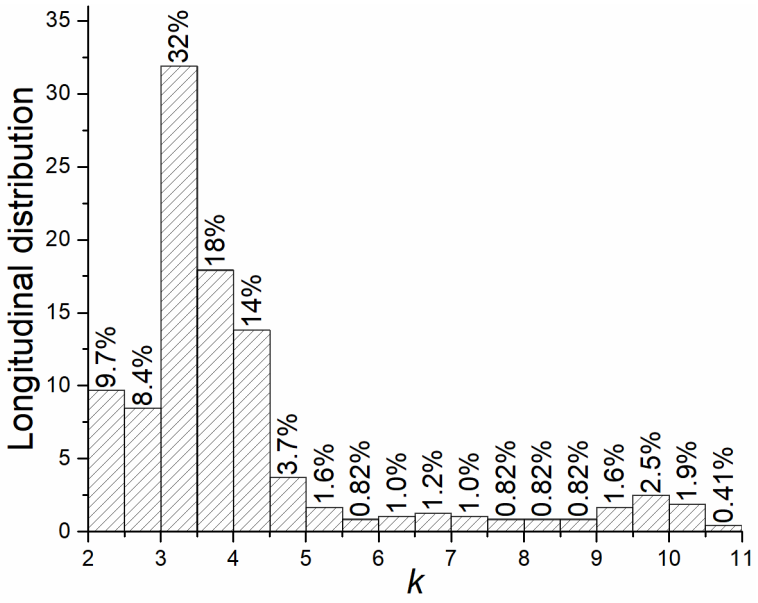


643

644 Figure 17 Frequency of the parameter *k* for the general corrosion part of the steel bar along

645 the longitudinal direction

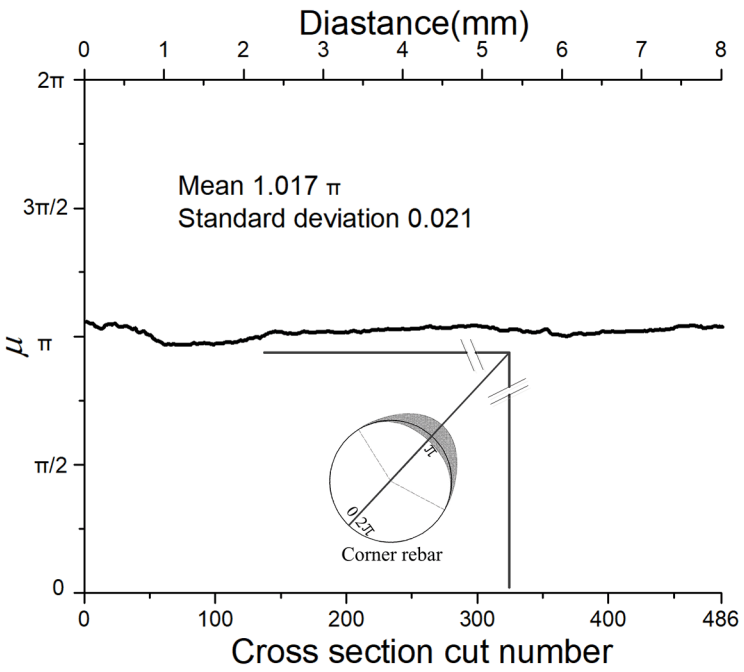


646

647 Figure 18 Locations of the maximum thickness of the rust in the polar coordinate system

648

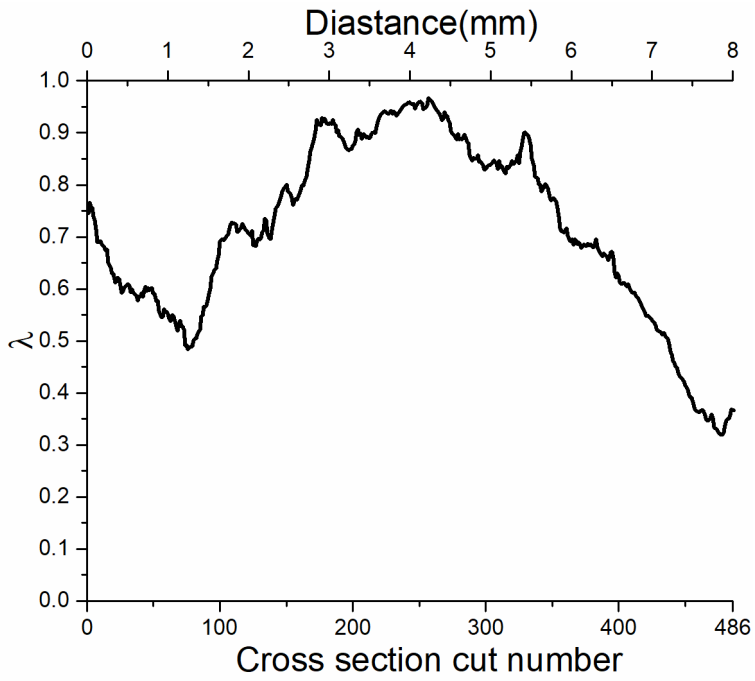


649

650 Figure 19 Fitting parameter $\lambda$ for the general corrosion part of the steel bar along the

651 longitudinal direction

652

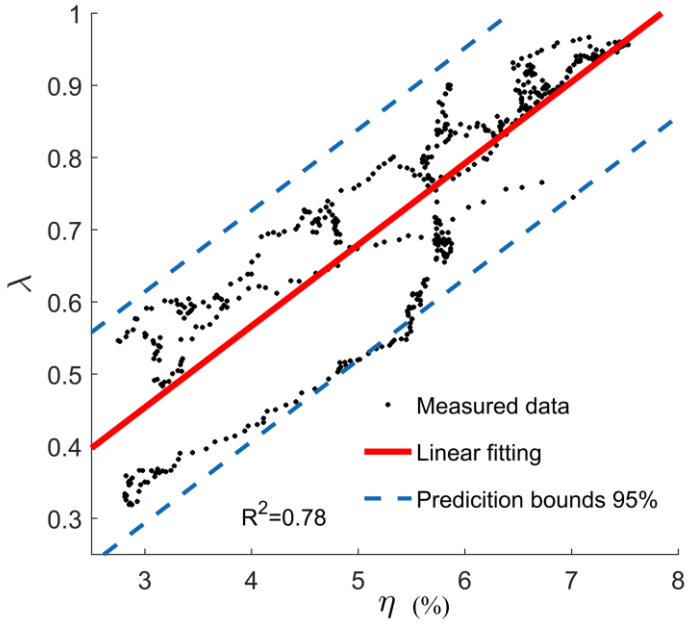


653

654 Figure 20 Relationship between the corrosion degree $\eta$ and the fitting parameter $\lambda$